Research Article | Vol. 28, No. 1 / 6 January 2020 / Optics Express 334
Optics EXPRESS

Linear and nonlinear spin-orbital coupling in golden-angle spiral quasicrystals

KAIKUN NIU,[1,2] MING FANG,[1,2] XINGANG REN,[1,2] ZHIXIANG HUANG,[1,2,5] HAO REN,[1,2] XIANLIANG WU,[1,2] AND WEI E. I. SHA[3,4]

[1]*Institute of Physical Science and Information Technology, Anhui University, Hefei 230601, China*
[2]*Key Laboratory of Electromagnetic Environmental Sensing, Department of Education of Anhui Province, Hefei 230601, China*
[3]*Key Laboratory of Micro-nano Electronic Devices and Smart Systems of Zhejiang Province, College of Information Science & Electronic Engineering, Zhejiang University, Hangzhou 310027, China*
[4]*weisha@zju.edu.cn*
[5]*zxhuang@ahu.edu.cn*

Abstract: The appealing characteristics of quasi-crystalline nanostructure offer tremendous possibilities to tailor the transmission of the angular momenta. Moreover, the second harmonic generation existing in nonlinear nanostructures also exhibits remarkable potential in the fundamental and applied research areas of the angular momenta conversion. By systematically studying the general angular momenta conservation law, we show that the high-dimensional angular momenta transformation and spin-orbital coupling are realized by the nonlinear sunflower-type quasicrystals, which feature the high-fold rotational symmetry and possess an increasing degree of rotational symmetry in Fourier space. Interestingly, since the sequential Fibonacci numbers are essentially encoded in the distinctive nonlinear sunflower-type patterns, the high-fold angular momenta transformation regularly occurs at both linear and nonlinear wavelengths. The investigations of fundamental physics for the unique quasi-crystals reveal scientific importance for manipulating the angular momenta of nonlinear optical signals, which plays a key role in the promotion and development of modern physics.

1. Introduction

Over the past few years, it has been confirmed that in addition to periodic structures, a broad range of aperiodic structures [1–3], which lie between periodic and disordered structures, have attracted a great deal of interest due to its conspicuous flexibility, and high feasibility of various appealing optical phenomena. Especially, a new cluster of ordered atomic structures with quasi-periodicity has been defined as quasi-crystals [4,5], which possess more subtle long-range translational order and orientational order as compared with the other two classes of solid state: crystalline and amorphous structures. Photonic quasicrystals can also be regarded as deterministic quasiperiodic crystals, which feature self-similarity, exhibit discrete Fourier components, support long-range order, lack translational symmetry and can be constructed to obey deterministic generation rules. Moreover, it is obvious that the property of the symmetry for the crystals determines the isotropy of photonic bandgap. According to a well-known optical theorem [4], in order to realize the complete bandgap and enable the Brillouin zone more circular, the level of symmetry must be enhanced. It is unfortunate that the highest order of symmetry in conventional periodic lattices is six-fold and all of the high-fold symmetry axes are forbidden, which is tough to maintain the isotropy of the optical system by inhibiting the orientational order. Therefore, more complicated and functional quasi-crystals with a higher level of symmetry are imminently required to break the aforementioned limitation. It is a remarkable fact that the sunflower-type [1,2,6] (i.e., golden-angle spiral array) quasi-crystal which follows a special golden angle spiral

#373957 https://doi.org/10.1364/OE.373957
Journal © 2020 Received 29 Jul 2019; revised 20 Oct 2019; accepted 11 Dec 2019; published 2 Jan 2020

Optics EXPRESS

arrangement has been investigated intensively in the context of aperiodic structures. It not only possesses the advantage of traditional quasi-crystals but also has some unique characteristics, such as the high-fold rotational symmetry, isotropic bandgap and continuous circular symmetry ring in reciprocal space. As a consequence, the structure of sunflower-type quasi-crystal is of significant interest and shows particularly potential applications like circular photonic crystal micro-cavity [7], bent waveguides [8] and spectrometer [9]. The development of golden-angle spiral quasi-crystal, which is a momentous branch of aperiodic structures, has also opened up the promising possibilities for advancing the research in the field of photonics and optics.

On the other hand, a myriad of nonlinear optical characteristics [10–13] has been extensively engineered and studied in modern photonic functionalities by optical approaches. In particular, second-harmonic generation (SHG) [14,15] plays a key role in the enormous fundamental and applied research areas, including nonlinear imaging [16], nonlinear sensing [17] and terahertz source generation [18]. To the best of our knowledge, the investigation of SHG in golden-angle spiral arrays is rarely reported. Thus, it is of great interest to explore the relationship between the second-order nonlinear processes and the high-fold rotational symmetry of aperiodic nanostructure, which will be of critical importance to understand the underlying physical mechanism of quasi-crystals, and offer the in-depth insight to design the aperiodic nonlinear optical devices which can tailor the angular momentum. There are two kinds of angular momentum: the spin angular momentum (SAM) and the orbital angular momentum (OAM). The SAM is carried by the circularly polarized wave. The left-handed/right-handed circular polarization describes the spin characteristic of photon and per photon contains a SAM of +/− $\hbar$, where $\hbar$ is known as the reduced Planck constant. OAM manifested by the helical wavefront of light and the orbital rotation of photon. Each of its photons has an OAM of $l\hbar$, where l is the azimuthal mode index and can be any integer. The total angular momentum is the sum of the SAM and OAM. As we know, angular momentum [19,20], the rotational equivalence of linear momentum carried by electromagnetic wave, is a conserved quantity (i.e. the total sum of angular momentum in a closed system remains constant). However, while the electromagnetic wave carrying angular momentum irradiate the scatterer, the angular momentum of the scattered or radiated wave will be altered due to the phase change at the scatterer. The change regularity depends on the properties of the scatterer and also obeys the general angular momenta conservation law [21]. The transfer of angular momentum has given rise to a new understanding of various developments and research areas ranging from quantum information, spatial light modulators, microscopy to hologram design [22,23]. It also opens unprecedented and potential perspectives for the applications of optical communication [24,25], nanometrology [26], super resolution imaging [27] and optical tweezers [28].

In this work, we theoretically formulate the general angular momenta conservation law [21] to reveal the optical properties of a sunflower-type nonlinear metallic quasi-crystal. Specifically, the consecutive Fibonacci numbers ($N = 0$, 1, 1, 2, 3, 5, 8, 13, 21...) are encoded in the unique golden-angle spiral array which features high-fold rotational symmetry. Through illuminating a circularly polarized light beam on the sunflower-type pattern to analyze both the linear and nonlinear responses, our results show that the high-dimensional angular momenta transformation and spin-orbital coupling can be observed at both fundamental and second-harmonic frequencies. Furthermore, to reveal the fundamental and SHG processes in such a complex structure, we propose the self-consistent and multi-physical framework [29,30] involving finite-difference time-domain (FDTD) - compatible discretization [31–33] for the Maxwell-hydrodynamic equations [34,35]. The non-perturbative time-domain model immaculately captures the nonlinear optical behaviors of free-electron gas in metals, opening opportunities to account for both linear and nonlinear dynamics in metallic quasi-crystals.

Optics EXPRESS

2. Model and method

Firstly, to achieve the high-fold transformation of spin and orbital angular momenta, the pattern of sunflower head with high-fold symmetry will be considered (as shown in Fig. 1(a)). As we know, the flower and seed pattern of the sunflower head is one of the Fermat's spiral forms and can be described by a particular generation rule, which was firstly proposed by Vogel in 1979 [2]. Here, the generation rule [36] in polar coordinate can be implemented as

$$r = k\sqrt{n} \tag{1}$$

$$\theta = n\varphi \tag{2}$$

where r and θ represent spatial positions of flower or seed in the sunflower head in polar coordinates, n is an integer (i.e., $n = 0, 1, 2, \ldots$) standing for the number of seeds in a sunflower head, φ is known as the golden angle or Fibonacci angle, which gives the constant aperture between adjacent position vectors r (n) and r $(n+1)$ of particles in the spiral arrays. For the sunflower-type spiral, it can be defined as $\varphi = 360/\alpha^2 \approx 137.508°$, where $\alpha = \left(1 + \sqrt{5}\right)/2 \approx 1.618$ is the golden ratio, and k represents the scaling factor. The sunflower head spiral can be regarded as a golden angle spiral, and the most remarkable characteristic of the structure is that the pattern can be decomposed into two sets of arcs or parastichies, one running clockwise, the other counterclockwise. In addition, it is noteworthy that the number of arcs in two families also follows invariably two consecutive numbers of the Fibonacci sequence. The golden ratio α is rationally approximated by the ratio of the numbers of parastichies (p/q), and the formula 360 / $(1+ p/q)\ \alpha^{-1}$ approximates the golden angle φ. Thus, the arrangement of florets in the sunflower head is also known as a golden-angle spiral array. Furthermore, since the Fibonacci angle φ is an irrational number, the sunflower head spiral is neither traditional rotational nor translational symmetry structure. Interestingly, the sunflower spiral has the distinctive feature of high-fold rotational symmetry, when the unique spiral pattern is encoded in the consecutive Fibonacci numbers (N = 0, 1, 1, 2, 3, 5, 8, 13, 21. . .). As a result, the high-fold transformation of spin and orbital angular momenta can be achieved by sunflower spiral pattern.

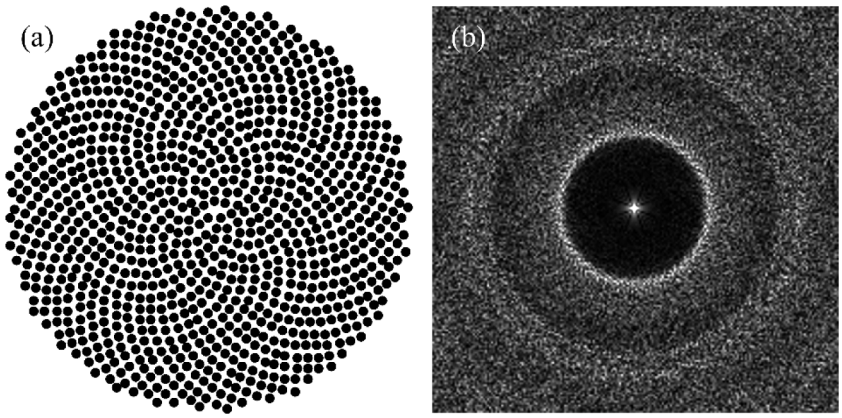

Fig. 1. (a) Schematic of the sunflower spiral arrays. (b) Discrete Fourier transforms (DFT) of the sunflower spiral arrays.

To better realize the diffraction properties of the plasmonic sunflower-type pattern, it is of significant importance to explore the structure related to reciprocal space vectors (i.e. Fourier space), which can be obtained by Discrete Fourier transforms (DFT) [37]. Figure 1(a) depicts the spatial space of the sunflower-type pattern with $n = 1000$ particles obeying the generation rule

Optics EXPRESS

according to Eqs. (1) and (2), and Fig. 1(b) illustrates the Fourier space of the sunflower spiral arrays by applying DFT to Fig. 1(a). Accordingly, the Vogel spirals is lack of rotational symmetry, and the spatial Fourier spectrum of deterministic sunflower arrays does not exhibit well-defined Bragg peaks, but rather possesses a diffusive character with highly isotropic, and approaches an increasing degree of continuous circular symmetry (i.e., support circularly symmetric scattering ring), due to the high degree of statistical isotropy. The symmetric scattering ring discovered in the Brillion zone is the origin of the spin-orbital coupling, which is carried by the circular scattering resonances in the golden angle spiral quasi-crystals.

Additionally, due to the nonlinear properties of metallic quasi-crystal, the FDTD method is employed to theoretically solve the hydrodynamic-Maxwell equations, which enables self-consistent numerical investigation of linear and nonlinear interaction between light and metallic nanostructures. It should be emphasized that this universal and non-perturbative hydrodynamic model used here describes a free electron gas in metals and is free from any approximations. The convective acceleration and the magnetic contribution of the Lorenz force terms in the hydrodynamic model contribute to the generation of multiple harmonic. In addition, the nonlocal effect is also taken into account by the quantum electron pressure term. As a result, the high-order harmonic generation can be governed by the conservation laws of charge, energy and angular momentum.

In this case, we propose to use a pure scattered field technique and investigate the propagation of the electromagnetic field, the general Maxwell's formulae are given by

$$\nabla \times \mathbf{E}_{sca} = -\mu_0 \frac{\partial \mathbf{H}_{sca}}{\partial t} \tag{3}$$

$$\nabla \times \mathbf{H}_{sca} = \mathbf{J} + \varepsilon_0 \frac{\partial \mathbf{E}_{sca}}{\partial t} \tag{4}$$

where ε_0 and μ_0 represent the vacuum permittivity and permeability, $\mathbf{J}$ is the polarization current. $\mathbf{E}_{\mathrm{sca}}$ and $\mathbf{H}_{\mathrm{sca}}$ are the scattered electric and magnetic fields produced by the polarization current. In addition, hydrodynamic and current continuity equations are defined to model SHG from the metal nanostructure:

$$\frac{\partial \mathbf{v}}{\partial t} + \mathbf{v} \cdot \nabla \mathbf{v} + \gamma \mathbf{v} = -\frac{e}{m}(\mathbf{E}_{inc} + \mathbf{E}_{sca} + \mu_0 \mathbf{v} \times (\mathbf{H}_{inc} + \mathbf{H}_{sca})) + \nabla V_P \tag{5}$$

$$\frac{\partial n}{\partial t} = -\nabla \cdot (n\mathbf{v}), \mathbf{J} = -en\boldsymbol{\nu} \tag{6}$$

where e and m are the elementary charge and electron mass. $\mathbf{E}_{\mathrm{inc}}$ and $\mathbf{H}_{\mathrm{inc}}$ are the incident electric and magnetic fields produced by the plane wave source. $\mathbf{v}$ and n are the electron velocity and density, respectively. It is particularly worth mentioning that $\mathbf{v}$ and n are both position and time-dependent. Regarding the boundary conditions, the normal component of electron velocity $\mathbf{v}$ at the boundary of metal is set to zero. The overall electron charges within the metal nanostructure N_{total} is a constant and associated with the initial electron density n_0. $\mathbf{v}\cdot\nabla\mathbf{v}$ is the convective acceleration term and γ is the scattering rate (related to the loss term). $\mathbf{v}\cdot\nabla\mathbf{v}$, $n\mathbf{v}$, and $\mathbf{v}\times\mathbf{H}$ terms have been incorporated to fully describe the nonlinear effect. The potential V_{p} including Hartree, exchange, Fermi, and Bohm potentials underlies the physical origins of the nonlocal and quantum effects, which can be ignored for the nanostructure with a size typically larger than 10 nm. The complete hydrodynamic model employed in this paper can accurately capture both the linear and nonlinear dynamics of the conduction free electrons. Meanwhile, it also can account for the nonlocal effect in the full-wave time-domain simulation, which is much more valuable as compared to the traditional Drude model. The size of each element in the golden angle spiral quasicrystals is basically larger than 10 nm, thus we mainly concentrate on the nonlinear dynamics of the conduction electrons in the metal. These powerful capacities make

Optics EXPRESS

hydrodynamic-Maxwell model promising for simulation and investigation of nonlinear responses from metals.

Figure 2 depicts the schematic of the metallic sunflower-type quasi-crystal pattern with high-fold rotational symmetry, which is composed of several metallic nanopillars and surrounded by air. On the basis of previous theoretical studies, it is evident that there are two classes of parastichies are displayed in the golden angle spiral of the sunflower head; and the number of clockwise (red line) and counterclockwise (blue line) parastichies are exactly satisfied as two successive (one after the other) Fibonacci Numbers, e.g. $p = 13$ (red) and $q = 21$ (blue) spirals are arranged for the sunflower pattern in this work as illustrated in Fig. 2. It is fancy that the ratio of two consecutive numbers of the Fibonacci sequence is also very close to the golden ratio. Moreover, the nonlinear properties of the metal are described by the aforementioned full hydrodynamic model, the parameters are chosen as $n_0 = 5.98\times10^{28}$ m^{-3} and $\gamma = 1.075\times10^{14}$ s^{-1}. To ensure the plasmon resonance of nanopillar locating in the optical frequency region, the geometrical parameters of the nanopillar have been optimized and the resonance wavelength is engineered at 780 nm by simulating the normalized scattering cross section of the nanopillar (shown in Fig. 3). The inset of Fig. 3 shows the dimension of the nanopillar ($r = 143$ nm and $h = 50$ nm). The quasi-crystal is irradiated by the circularly polarized light beam, whose central wavelength is also selected as 780 nm. As a result, the signals located at the fundamental wavelength (780 nm) and second harmonic wavelength (390 nm) both can be detected. In the simulation, the perfectly matched layers (PMLs) are employed in the x-, y- and z-directions to truncate the boundaries of the calculation domain in the FDTD scheme. The uniform spatial and temporal steps are adopted as $\Delta x = \Delta y = \Delta z = 2.5 \times 10^{-9}$ m and $\Delta t = 8.33 \times 10^{-18}$ s, respectively. The input source is set as:

$$E(t) = E_0 \exp\left(-0.5\left(\frac{t - t_0}{\tau}\right)^2\right)\cos(2\pi f t) \tag{7}$$

where E_0 is the amplitude and τ is the bandwidth of the source, respectively. To ensure the excitation of the nonlinear response, the source should essentially have an extremely high

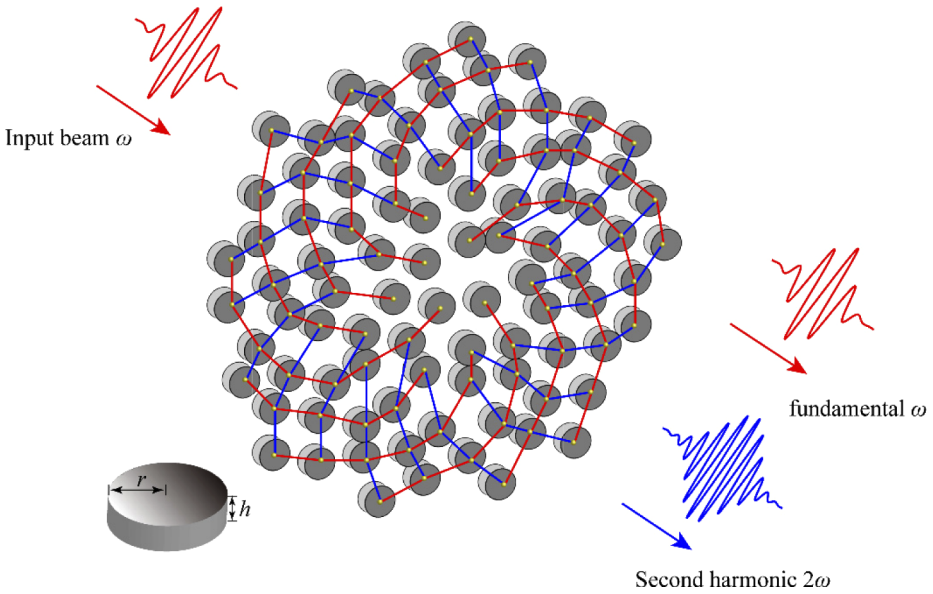

Fig. 2. Schematic of second-harmonic generation (SHG) with the sunflower spiral arrays.

Optics EXPRESS

amplitude and especially narrow bandwidth. Hence, $E_0 = 1 \times 10^7$ V/m and $\tau = 20 \times 10^{-5}$ s and $t_0 = 3\ \tau$ are selected in this circumstance.

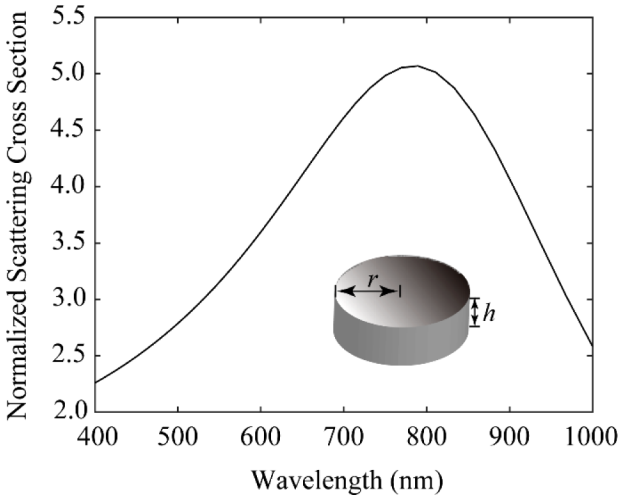

Fig. 3. The normalized scattering cross section of the nanopillar. The inset is the illustration of the nanopillar.

3. Results and discussion

Next, we continue our study by analyzing the general angular momenta conservation law. We will consider the incident field carrying with the spin and orbital angular momenta, which irradiates on the nanostructures with N-fold rotational symmetry. Our goal is to demonstrate the transfer of angular momenta from the incident beam to the scattered field during both linear and nonlinear interaction processes in our proposed N-fold rotational symmetry nanostructures. The general angular momenta conservation law is given by:

$$j_{sca} = s(l + \sigma) + qN \tag{8}$$

where j_{sca} denotes the total angular momenta number of the scattered field, s is the order of harmonic generation ($s = 1$ for linear processes, $s = 2$ for SHG, $s = 3$ for third-harmonic generation, etc.), l represents orbital momentum numbers ($l = 0, \pm1, \pm2, \pm3$, etc.) and σ is the spin angular momentum numbers ($\sigma = -1$ for left-circularly polarized, $\sigma = 1$ for right circularly polarized) of the incident field, respectively. q is an integer ($q = 0, \pm1, \pm2, \pm3$, etc.) and N is the quasi-angular-momentum number of the N-fold rotational symmetry nanostructure.

To demonstrate the validation of this general angular momenta conservation law, the total angular momenta of the scattered fundamental and SH fields from the independent nanopillar and sunflower-type quasicrystal are analyzed by the multipole expansion method [38]. Firstly, we consider a single gold nanopillar ($N = 0$) with a radius of $r = 143$ nm and a height of $h = 50$ nm illuminated by the right-circularly polarized incident beam (i.e. $l = 0$ and $\sigma = -1$). The resonance of the nanopillar is fixed to 780 nm. The total angular momenta have been investigated to unveil the relative contributions of the electric and magnetic multipoles (MM and EM) to the scattered fields, the fundamental and second-harmonic scattered waves from a golden cylinder are decomposed into diverse angular momentum channels. Figure 4 demonstrates the relative contributions of the electric and magnetic multipoles to the total angular momenta of the fundamental and second-harmonic scattered fields. According to Eq. (8), the quantum numbers of the total optical angular momenta for the scattered fundamental field ($s = 1$) are $j_{\mathrm{sca}} = 1 \times$

Optics EXPRESS

$(-1+0) = -1$ (see Figs. 4(a) and 4(b)). Considering the scattered second harmonic field ($s = 2$), the quantum numbers are $j_{sca} = 2 \times (-1+0) = -2$ (see Figs. 4(c) and 4(d)). The analytical predictions, based on the general angular momenta conservation law, significantly agree well with the multipole decomposition weights of the total angular momenta of the scattered fundamental and second-harmonic fields (as shown in Fig. 4). Besides, to further understand the underlying physics, Figs. 5(a)–5(d) illustrate the electric and magnetic multipole resonance L, which satisfies $L \geq |\, j_{sca} \,|$. For the linear process, the nanopillar is irradiated by the plane wave, the electric dipole (Fig. 5(b)), magnetic dipole and quadrupole (Fig. 5(a)) exist. For the SHG process, the surface nonlinear source generated resembles the dipole source. As a result, several higher-order

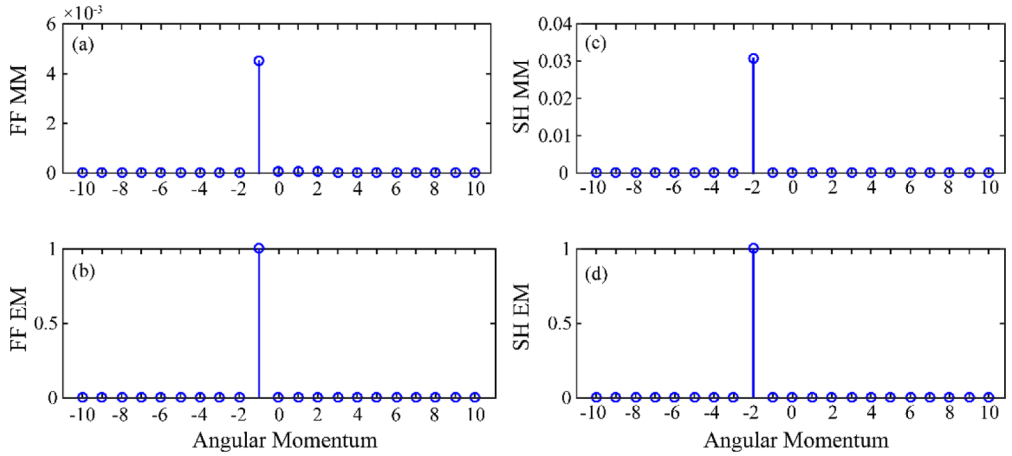

Fig. 4. Multipolar decompositions of the fundamental and second-harmonic scattered waves from the gold nanopillar in terms of angular momenta channels. MM and EM denote magnetic multipole and electric multipole, respectively. The nanopillar is illuminated by the right circularly polarized (RCP) beam. (a) and (b) correspond to scattered waves at the fundamental frequency (FF), whereas (c) and (d) correspond to wave scattering at second harmonic (SH).

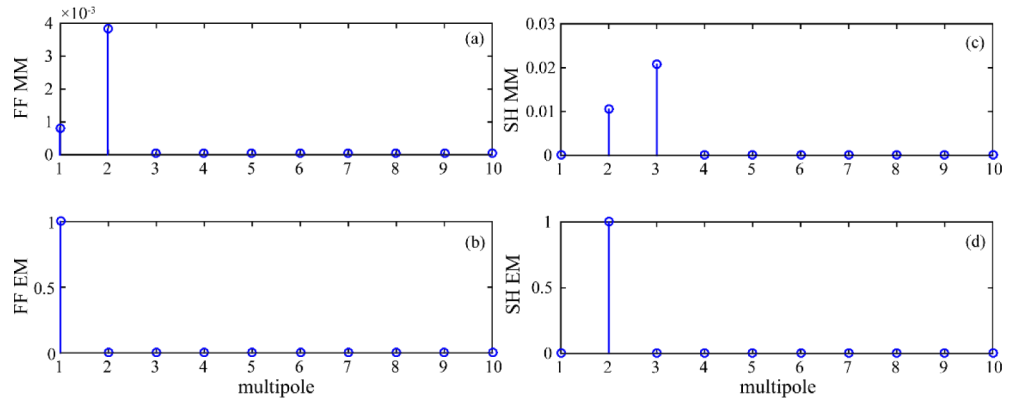

Fig. 5. The electric and magnetic multipole resonances of the fundamental and SH scattered waves from the gold nanopillar. MM and EM denote magnetic multipole and electric multipole, respectively. The nanopillar is illuminated by the right circularly polarized (RCP) beam. (a) and (b) correspond to scattered waves at the fundamental frequency (FF), whereas (c) and (d) correspond to wave scattering at second harmonic (SH).

Optics EXPRESS

modes including the electric quadrupole (Fig. 5(d)), magnetic quadrupole and octupole (Fig. 5(c)) are excited.

To further unveil the angular momenta transformation of both fundamental and second-harmonic fields, the fascinating golden-angle spiral array has been simulated by the FDTD method and post-possessed by the multipole expansion method. The angular momenta conservation law is theoretically studied to guarantee its universality. Considering the computational efficiency, the sunflower-type metallic quasi-crystal is composed of one hundred identical nanopillars and the dimensions of the nanopillars are the same as the one in the above section. The incident right circularly polarized (RCP) beam has $l = 0$ and $\sigma = -1$, the quantum numbers of the total optical angular momenta for the golden angle spiral array can be determined according to the general angular momenta conservation law. Firstly, for the scattered fundamental field ($s = 1$), the quantum numbers can be obtained as $j_{sca} = 0, 1, 1, 2, 3, 5, 8, 13 + 1 \times (-1 + 0) = -1, 0, 1, 2, 4,$

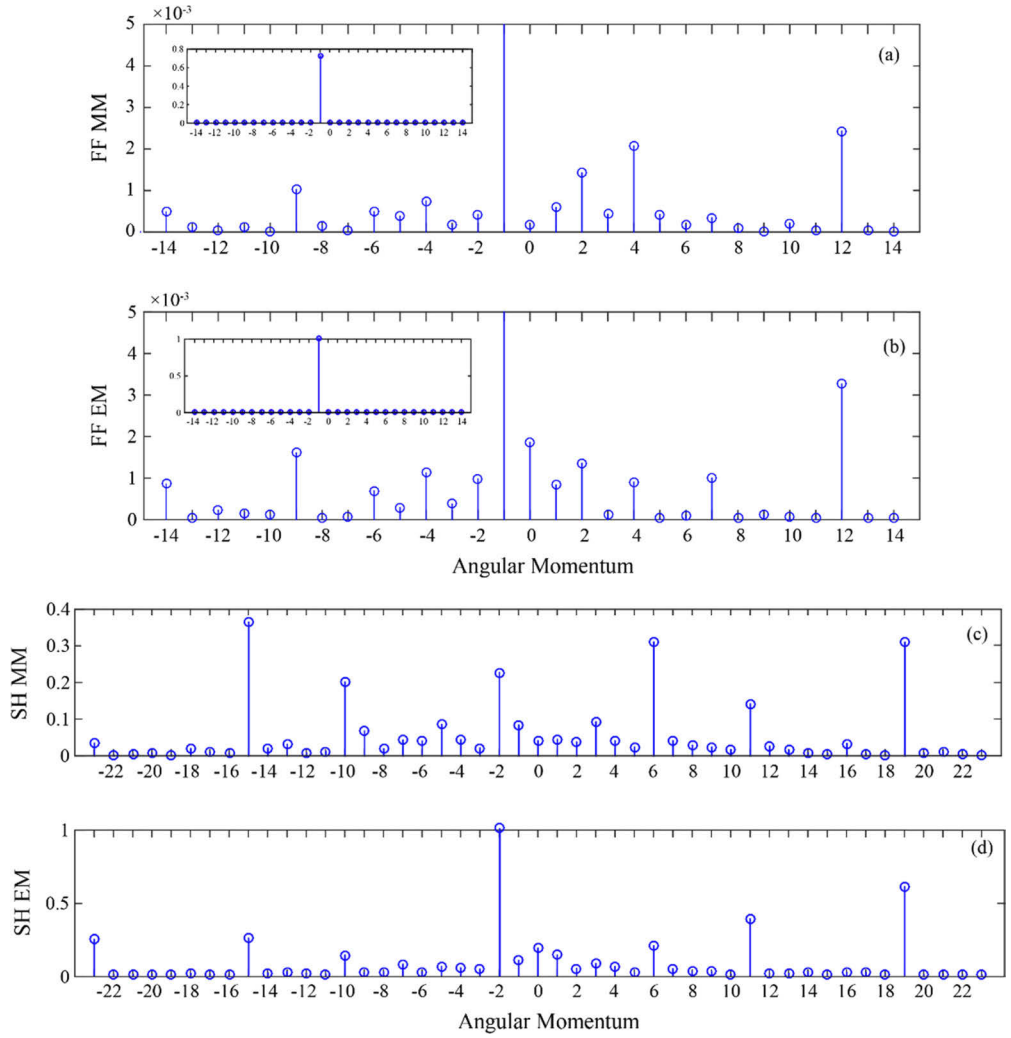

Fig. 6. Multipolar decompositions of the fundamental and second-harmonic scattered waves from the golden sunflower in terms of angular momenta channels. The sunflower is illuminated by the RCP beam. (a) and (b) correspond to scattered waves at the fundamental frequency (FF), whereas (c) and (d) correspond to wave scattering at second harmonic (SH).

Optics EXPRESS

7, 12 and j_{sca} = -1, -1, -2, -3, -5, -8, -13 + 1 × (-1 + 0) = -2, -3, -4, -6, -9, -14. For the scattered SH field (s = 2), the quantum numbers can be determined as j_{sca} = 0, 1, 1, 2, 3, 5, 8, 13, 21 + 2 × (-1 + 0) = -2, -1, 0, 1, 3, 6, 11, 19 and j_{sca} = -1, -1, -2, -3, -5, -8, -13, -21 + 2 × (-1 + 0) = -3, -4, -5, -10, -15, -23.

Figure 6 demonstrates the relative contributions of the electric and magnetic multipoles to the total angular momenta of the scattered fields for the sunflower-type quasicrystal. Figures 6(a) and 6(b) correspond to the magnetic multipole and electric multipole at FF, respectively, whereas Figs. 6(c) and 6(d) correspond to the magnetic multipole and electric multipole at second harmonic, respectively. As shown in Fig. 5, the rotational symmetry properties influence the transformation of optical angular momenta from incident beam to the scattered fields at both fundamental and second-harmonic wavelengths. Interestingly, the golden angle spiral array with high-fold rotational symmetry supports distinctive optical resonances that encode Fibonacci numbers, and the phenomena of high-dimensional transfer of angular momenta can be well captured, which leads to the coupled spin and orbital angular momenta conversion in the system. Our simulation results also perfectly agree with the predictions of the general angular momenta conservation law. As shown in the inset of Figs. 6(a) and 6(b), for the linear condition, the -1 channel of the angular momentum is dominated, which is similar to the single gold nanopillar (Fig. 4(a) and 4(b)). As a result, the amplitude of the -1 channel of the angular momentum is much larger than other channels. However, the sunflower-type pattern has a major impact on the angular momenta channels in the nonlinear process, which results in the amplitudes of all channels are on the same order of magnitude as shown in Figs. 6(c) and 6(d).

The spatial distributions of the near-field electric field intensity $|E|^2$ scattered from a nanopillar (top panels) and sunflower-type quasi-crystal (bottom panels) at the fundamental (λ = 780 nm)

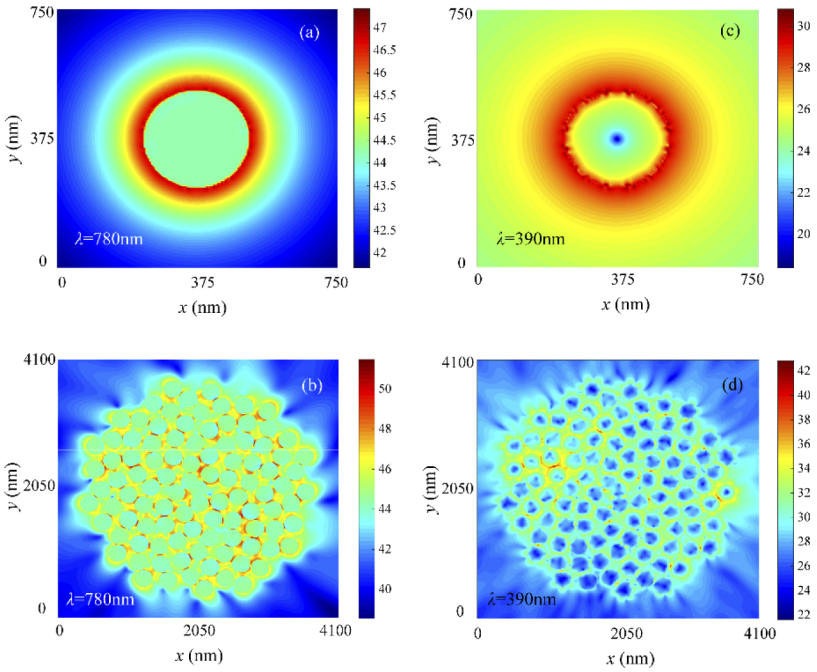

Fig. 7. Electric field intensity $|E|^2$ in vertical crosscuts through the individual nanopillar (top panels) and the sunflower-type quasicrystal (bottom panels), respectively. (a) and (b) correspond to near-field at the fundamental frequency (780 nm), whereas (c) and (d) correspond to near-field at second harmonic (390 nm).

Optics EXPRESS

and SH wavelength ($\lambda = 390$ nm) are illustrated in Fig. 7. The electric fields are recorded in the cross-section perpendicular to propagation direction and presented on a logarithmic scale. As shown in Fig. 7(a) for the individual nanopillar, the local electric fields are confined around the surface of nanopillar due to the effect of surface plasmon resonance at the linear wavelength. As we know, the nonlinear signal is driven by the surface-induced multipolar source and affected by the near-field distribution and surface plasmon resonance, but it would be much weaker than the linear signal. Hence, the electric fields in Fig. 7(c) are also concentrated on the surface but with much lower amplitude at the nonlinear wavelength. For the sunflower-type quasicrystal, besides the strong surface electric fields, the local fields are also enhanced at the junction areas of different nanopillars because of the intensive coupling between nanopillars. Therefore, the amplitudes of E-field of the quasicrystal are significantly enlarged as compared to the individual nanopillar as shown in Figs. 7(b) and 7(d).

4. Conclusion

In conclusion, we surveyed the general angular momenta conservation law, and demonstrate the manipulation of the linear and nonlinear spin-orbital interactions by the sunflower-type quasi-crystals, which feature high-fold rotational symmetry. Surprisingly, while the quasicrystals are excited by the circularly polarized input beam only carrying low spin angular momentum, the consecutive Fibonacci number encoded in the pattern is converted into the total angular momenta of the scattering field. In other words, the spin-orbital coupling and the high-fold angular momenta transformation can be realized in the system simultaneously. Our results have significant scientific importance, particularly to exploit nonlinear quasi-crystal and manipulate the spin and orbital angular momenta in the nanophotonics field, as well as other research areas.

Funding

National Natural Science Foundation of China (61601166, 61701001, 61701003, 61701423, 61701424, 61871001, 61971001, 61975177, 61402090608); Natural Science Foundation of Anhui Province (1808085QF179); National Outstanding Youth Science Fund Project of National Natural Science Foundation of China (61722101); Thousand Talents Program for Distinguished Young Scholars of China; Marie Sklodowska-Curie Individual Fellowship (MSCA-IFEF-ST(752898)); China Scholarship CouncilOpen fund for Discipline Construction, Institute of Physical Science and Information Technology, Anhui University.

References

1. N. Lawrence, J. Trevino, and L. Dal Negro, "Aperiodic arrays of active nanopillars for radiation engineering," J. Appl. Phys. **111**(11), 113101 (2012).
2. H. Vogel, "A better way to construct the sunflower head," Math. Biosci. **44**(3-4), 179–189 (1979).
3. Z. V. Vardeny, A. Nahata, and A. Agrawal, "Optics of photonic quasicrystals," Nat. Photonics **7**(3), 177–187 (2013).
4. M. Zoorob, M. Charlton, G. Parker, J. Baumberg, and M. Netti, "Complete photonic bandgaps in 12-fold symmetric quasicrystals," Nature **404**(6779), 740–743 (2000).
5. D. Levine and P. J. Steinhardt, "Quasicrystals: a new class of ordered structures," Phys. Rev. Lett. **53**(26), 2477–2480 (1984).
6. A. Agrawal, N. Kejalakshmy, J. Chen, B. Rahman, and K. Grattan, "Golden spiral photonic crystal fiber: polarization and dispersion properties," Opt. Lett. **33**(22), 2716–2718 (2008).
7. P.-T. Lee, T.-W. Lu, J.-H. Fan, and F.-M. Tsai, "High quality factor microcavity lasers realized by circular photonic crystal with isotropic photonic band gap effect," Appl. Phys. Lett. **90**(15), 151125 (2007).
8. N. Horiuchi, Y. Segawa, T. Nozokido, K. Mizuno, and H. Miyazaki, "High-transmission waveguide with a small radius of curvature at a bend fabricated by use of a circular photonic crystal," Opt. Lett. **30**(9), 973–975 (2005).
9. B. Redding, S. F. Liew, R. Sarma, and H. Cao, "Compact spectrometer based on a disordered photonic chip," Nat. Photonics **7**(9), 746–751 (2013).
10. C. G. Biris and N. C. Panoiu, "Nonlinear surface-plasmon whispering-gallery modes in metallic nanowire cavities," Phys. Rev. Lett. **111**(20), 203903 (2013).
11. C. Biris and N. Panoiu, "Second harmonic generation in metamaterials based on homogeneous centrosymmetric nanowires," Phys. Rev. B **81**(19), 195102 (2010).

Optics EXPRESS

12. N. Panoiu, W. Sha, D. Lei, and G. Li, "Nonlinear optics in plasmonic nanostructures," J. Opt. **20**(8), 083001 (2018).
13. J. Sun, Y.-J. Gu, D. Y. Lei, S. P. Lau, W.-T. Wong, K.-Y. Wong, and H. L.-W. Chan, "Mechanistic understanding of excitation-correlated nonlinear optical properties in MoS2 nanosheets and nanodots: the role of exciton resonance," ACS photonics **3**(12), 2434–2444 (2016).
14. X. Y. Xiong, L. J. Jiang, E. Wei, Y. H. Lo, M. Fang, W. C. Chew, and W. C. Choy, "Strongly enhanced and directionally tunable second-harmonic radiation from a plasmonic particle-in-cavity nanoantenna," Phys. Rev. A **94**(5), 053825 (2016).
15. G. Li, S. Zhang, and T. Zentgraf, "Nonlinear photonic metasurfaces," Nat. Rev. Mater. **2**(5), 17010 (2017).
16. G. Bautista, M. J. Huttunen, J. Mäkitalo, J. M. Kontio, J. Simonen, and M. Kauranen, "Second-harmonic generation imaging of metal nano-objects with cylindrical vector beams," Nano Lett. **12**(6), 3207–3212 (2012).
17. J. Butet, I. Russier-Antoine, C. Jonin, N. Lascoux, E. Benichou, and P.-F. Brevet, "Sensing with multipolar second harmonic generation from spherical metallic nanoparticles," Nano Lett. **12**(3), 1697–1701 (2012).
18. M. Fang, K. Niu, Z. Huang, E. Wei, X. Wu, T. Koschny, and C. M. Soukoulis, "Investigation of broadband terahertz generation from metasurface," Opt. Express **26**(11), 14241–14250 (2018).
19. M. L. Chen, L. J. Jiang, and W. E. Sha, "Orbital angular momentum generation and detection by geometric-phase based metasurfaces," Appl. Sci. **8**(3), 362 (2018).
20. L. Allen, M. W. Beijersbergen, R. Spreeuw, and J. Woerdman, "Orbital angular momentum of light and the transformation of Laguerre-Gaussian laser modes," Phys. Rev. A **45**(11), 8185–8189 (1992).
21. X. Y. Xiong, A. Al-Jarro, L. J. Jiang, N. C. Panoiu, and E. Wei, "Mixing of spin and orbital angular momenta via second-harmonic generation in plasmonic and dielectric chiral nanostructures," Phys. Rev. B **95**(16), 165432 (2017).
22. S. Franke-Arnold, L. Allen, and M. Padgett, "Advances in optical angular momentum," Laser Photonics Rev. **2**(4), 299–313 (2008).
23. H. Ren, G. Briere, X. Fang, P. Ni, R. Sawant, S. Héron, S. Chenot, S. Vézian, B. Damilano, and V. Brändli, "Metasurface orbital angular momentum holography," Nat. Commun. **10**(1), 2986 (2019).
24. Y. Yan, G. Xie, M. P. Lavery, H. Huang, N. Ahmed, C. Bao, Y. Ren, Y. Cao, L. Li, and Z. Zhao, "High-capacity millimetre-wave communications with orbital angular momentum multiplexing," Nat. Commun. **5**(1), 4876 (2014).
25. H. Ren, X. Li, Q. Zhang, and M. Gu, "On-chip noninterference angular momentum multiplexing of broadband light," Science **352**(6287), 805–809 (2016).
26. Z. Yue, H. Ren, S. Wei, J. Lin, and M. Gu, "Angular-momentum nanometrology in an ultrathin plasmonic topological insulator film," Nat. Commun. **9**(1), 4413 (2018).
27. F. Tamburini, G. Anzolin, G. Umbriaco, A. Bianchini, and C. Barbieri, "Overcoming the Rayleigh criterion limit with optical vortices," Phys. Rev. Lett. **97**(16), 163903 (2006).
28. H. He, M. Friese, N. Heckenberg, and H. Rubinsztein-Dunlop, "Direct observation of transfer of angular momentum to absorptive particles from a laser beam with a phase singularity," Phys. Rev. Lett. **75**(5), 826–829 (1995).
29. K. Niu, Z. Huang, M. Fang, M. Li, X. Li, and X. Wu, "Coupling of Gain Medium and Extraordinary Optical Transmission for Effective Loss Compensation," IEEE Access **6**, 14820–14826 (2018).
30. H. Ren, X. Ren, Z. Huang, and X. Wu, "Synergetic light trapping effects in organic solar cells with a patterned semi-transparent electrode," Phys. Chem. Chem. Phys. **21**(21), 11306–11312 (2019).
31. K. Niu, Z. Huang, X. Ren, M. Li, B. Wu, and X. Wu, "An Optimized 3-D HIE-FDTD Method With Reduced Numerical Dispersion," IEEE Trans. Antennas Propag. **66**(11), 6435–6440 (2018).
32. K. Yee, "Numerical solution of initial boundary value problems involving Maxwell's equations in isotropic media," IEEE Trans. Antennas Propag. **14**(3), 302–307 (1966).
33. K. Niu, Z. Huang, M. Li, and X. Wu, "Optimization of the artificially anisotropic parameters in WCS-FDTD method for reducing numerical dispersion," IEEE Trans. Antennas Propag. **65**(12), 7389–7394 (2017).
34. P. Ginzburg, A. V. Krasavin, G. A. Wurtz, and A. V. Zayats, "Nonperturbative hydrodynamic model for multiple harmonics generation in metallic nanostructures," ACS Photonics **2**(1), 8–13 (2015).
35. M. Fang, Z. Huang, W. E. Sha, X. Y. Xiong, and X. Wu, "Full hydrodynamic model of nonlinear electromagnetic response in metallic metamaterials," Prog. Electromagn. Res. **157**, 63–78 (2016).
36. E. H. Lockwood, *A book of curves* (Cambridge University Press, 1967).
37. J. Trevino, H. Cao, and L. Dal Negro, "Circularly symmetric light scattering from nanoplasmonic spirals," Nano Lett. **11**(5), 2008–2016 (2011).
38. J. D. Jackson, *Classical electrodynamics* (Wiley, 1999).